Soft Matter

PAPER

View Article Online
View Journal | View Issue

Cite this: *Soft Matter*, 2023, **19**, 8221

Nature-inspired designs for disordered acoustic bandgap materials†

Xinzhi Li [a] and Dapeng Bi *[b]

We introduce an amorphous mechanical metamaterial inspired by how cells pack in biological tissues. The spatial heterogeneity in the local stiffness of these materials has been recently shown to impact the mechanics of confluent biological tissues and cancer tumor invasion. Here we use this bio-inspired structure as a design template to construct mechanical metamaterials and show that this heterogeneity can give rise to amorphous cellular solids with large, tunable acoustic bandgaps. Unlike acoustic crystals with periodic structures, the bandgaps here are directionally isotropic and robust to defects due to their complete lack of positional order. Possible ways to manipulate bandgaps are explored with a combination of the tissue-level elastic modulus and local stiffness heterogeneity of cells. To further demonstrate the existence of bandgaps, we dynamically perturb the system with an external sinusoidal wave in the perpendicular and horizontal directions. The transmission coefficients are calculated and show valleys that coincide with the location of bandgaps. Experimentally this design should lead to the engineering of self-assembled rigid acoustic structures with full bandgaps that can be controlled *via* mechanical tuning and promote applications in a broad area from vibration isolations to mechanical waveguides.

Received 29th March 2023,
Accepted 4th October 2023

DOI: 10.1039/d3sm00419h

rsc.li/soft-matter-journal

1 Introduction

A number of recent studies on mechanical metamaterials[1–10] with full acoustic bandgaps have attracted intense interests. These materials provide opportunities to precisely control propagations of mechanical waves and have a broad range of potential applications in vibration isolation,[11] acoustic cloaking,[12] wave filters,[13,14] waveguides[15,16] and mechanical switches.[4,17] Most of these studies have been devoted to the design and optimization of acoustic crystals,[1,2,5–10,18] which are periodic structural materials with full bandgaps. However, periodicity is not necessary for the formation of acoustic bandgaps (ABGs)[19,20] and amorphous structures with ABGs can offer many advantages over their crystalline counterparts. For example, amorphous acoustic materials can exhibit bandgaps that are directionally isotropic and are more robust to defects and errors in fabrications.[19,20] Currently, there are few existing protocols for designing amorphous acoustic materials. In a recent work by Ronellenfitsch *et al.*,[3] the authors investigate the acoustic bandgaps in a 2D disordered spring network constructed from Delanuary triangulation of randomly perturbed periodic unit cell. They show that the bandgap can be manipulated by optimizing distribution of stiffness of springs using machine learning methodologies. But the design is entirely artificial and the mechanism on how bandgaps arise is not well explored.

Biological tissue is sculpted by cell division, growth and rearrangements rather than artificial patterning. Therefore, biological cells naturally pack in a highly disordered manner, which is inherently non-crystalline.[21,22] Previous works have used biological structures to build amorphous photonic metamaterials[23] and topological mechanical materials.[24–26] Here, we propose a design for amorphous 2D ABG materials that is inspired by how cells pack in dense tissues in biology. We generate structures that exhibit broad ABGs based on a simple model that has been shown to describe cell shapes and tissue mechanical behaviors. An advantage of this design is that the width of ABGs can be directly tuned by single mechanical parameters. We also take advantage of the heterogeneity that is naturally-present in biological tissues. Based on the design protocol, we first study in-depth the static mechanical properties of the materials and characterize their acoustic spectrum and bandgaps. We then perform mechanical wave perturbations on these bio-inspired structures.

1.1 Cells form a natural disordered mechanical network in biological tissues

When epithelial and endothelial cells pack densely in 2D to form a confluent monolayer, the structure of the resulting tissue can be described by a polygonal tiling.[27] A great variety of cell shape structures have been observed in tissue monolayers, ranging from near-regular tiling of cells that resembles a dry foam or honeycomb lattice[28] to highly irregular tilings of

[a] *Department of Physics, Carnegie Mellon University, Pittsburgh, PA 15213, USA*
[b] *Department of Physics, Northeastern University, Boston, MA 02115, USA. E-mail: d.bi@northeastern.edu*

† Electronic supplementary information (ESI) available. See DOI: https://doi.org/10.1039/d3sm00419h

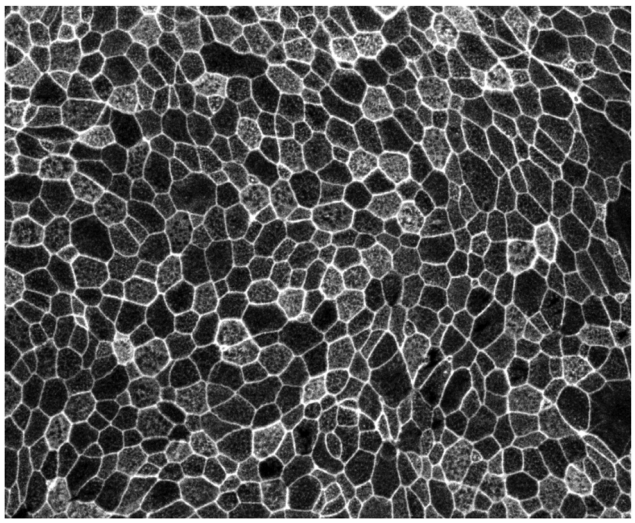

Fig. 1 Snapshot of a confluent epithelial tissue composed of mature, well-differentiated primary human bronchial epithelial cells grown in air–liquid interface culture.[32] Image Courtesy of the Park lab at the Harvard School of Public Health.

elongated cells.[29] Cells can interact with each other *via* mechanical forces and can transmit tensions at distances much larger than the single cell size.[30,31] Cells pack in a highly disordered way,[21,22] and form tissues by growth, apoptosis and rearrangements, which are all dynamical events. Thus the tissue is able to maintain a homeostatic balance and the cell shapes are largely maintained. In Fig. 1, we show a snapshot of primary human bronchial epithelial cells.[32]

2 Methods

2.1 Vertex model for generating amorphous cellular structures

To better understand how cell shapes arise from cell-level interactions, researchers have studied a simple vertex model[27,28] that incorporates the constraints on cell shapes imposed by confluence. The original models focused on 2D monolayers of cells, where the systems are coarse-grained as networks of cellular polygons that tessellate the plane. In the vertex model, the basic degrees of freedom are vertex positions of the polygons. The biomechanics of the tissue is governed by the energy function[27,28,33–37]

$$E = \sum_{i=1}^{N}\left[K_A\left(A_i - A_0^i\right)^2 + K_P\left(P_i - P_0^i\right)^2\right] \quad (1)$$

where cell areas $\{A_i\}$ and perimeters $\{P_i\}$ are functions of the position of vertices $\{\mathbf{r}_i\}$ and the connectivity between cells. K_A and K_P are the area and perimeter elasticities, respectively.

The term quadratic in cell area A_i results from cell volume incompressibility and the monolayer's resistance to height fluctuations.[28,33,35] Changes to cell perimeters are directly related to the deformation of the acto-myosin cortex concentrated near the cell membrane.[38,39] After expanding E, the term $K_P P_i^2$ corresponds to the elastic energy associated with deforming the cortex. The linear term in cell perimeter, $-2K_P P_0 P_i$, represents the effective line tension contributed by cell i which gives rise to a 'preferred perimeter' P_0. The value of P_0 can be decreased by up-regulating the contractile tension in the cortex of cell i[28,33,37,40] and it can be increased by up-regulating cell–cell adhesion between cell i and its neighbors. For this work, we will assume the individual preferred cell area A_0 does not vary from cell-to-cell and is set to be equal to the average area per cell (*i.e.* $A_0 = \bar{A}$), which also sets $\sqrt{\bar{A}}$ as the length unit. Therefore the unit of the tissue energy would be $K_P\bar{A}$. The tissue energy can be non-dimensionalized by $K_P A_0$ as the unit energy scale, $\varepsilon = \sum_{i=1}^{N}\left[\kappa_A(a_i-1)^2 + \left(p_i - p_0^i\right)^2\right]$, where $a_i = A_i/\bar{A}$ and $p_i = P_i\Big/\sqrt{\bar{A}}$ are the rescaled shape functions for area and perimeter of the ith cell. $\kappa_A = K_A\bar{A}/K_P$ is the rescaled cell area elasticity, and $p_0^i = P_0^i\Big/\sqrt{\bar{A}}$ is the preferred cell shape index.[37]

To capture the experimental heterogeneity in single-cell properties and in cell–cell interactions,[41–45] we introduce variations in the preferred shape indices $\{p_0^i\}$. The majority of this work uses a Gaussian distributed set of $\{p_0^i\}$ with mean μ and standard deviation σ. The results are insensitive to the form of distribution for $\{p_0^i\}$.[30,31] When the tissue heterogeneity $\sigma = 0$, all cells have the same preferred perimeter p_0 and the system becomes a homogeneous tissue which is well studied in previous works.[37,40] The open source code CellGPU[46] can be used to generate cellular structures and implement the vertex model simulations.

2.2 Characterizing the mechanical property of the cellular network

In this model, the cell stiffness is determined by the tension τ_m on cell–cell junctions (edges).[47–53] The tension of the edge m with length l_m shared by cells i,j is given by,[54,55]

$$\tau_m \equiv \frac{\partial E}{\partial l_m} = K_P\left[\left(p_i - p_0^i\right) + \left(p_j - p_0^j\right)\right]. \quad (2)$$

We also calculate the shear modulus[56] to quantify the rigidity on a tissue level.

To characterize the acoustic property of the system, we first calculate the Hessian matrix $H_{i\mu,j\nu} = \dfrac{\partial^2 E}{\partial r_i^\mu \partial r_j^\nu}$ and solve its engenvalues. By plotting the density of states (DOS), we could figure out the existence of bandgaps. To obtain the full band structure at various wave vectors $\boldsymbol{k}$, we calculate the eigenvalues of the dynamical matrix, which is the Fourier transform of the Hessian matrix. Considering a system with energy E, the equation of motion is

$$m_i \ddot{r}_i^\mu = -\frac{\partial E}{\partial r_i^\mu} = -\sum_{j\nu} H_{i,j}^{\mu,\nu} r_j^\nu. \quad (3)$$

Here $\boldsymbol{r}_i$ denotes the position of vertex i. $\mu = x,y$ are cartesian indices. We can assume periodic solutions to get the eigenvalue

equations

$$\omega^2 r_i^{\mu}(\boldsymbol{k}) = \sum_{j\nu} D_{i,j}^{\mu,\nu}(\boldsymbol{k}) r_j^{\nu}(\boldsymbol{k}). \tag{4}$$

Then the dynamical matrix is given by

$$D_{i,j}^{\mu,\nu}(\boldsymbol{k}) = \frac{1}{\sqrt{m_i m_j}} H_{i,j}^{\mu,\nu} \exp\left[-\mathrm{i}\boldsymbol{k}\cdot\left(\boldsymbol{R}_i^{\alpha} - \boldsymbol{R}_j^{\beta}\right)\right]. \tag{5}$$

For an amorphous structure, to calculate the dynamical matrix, the whole system is treated as a super unit cell containing multiple vertices. $\boldsymbol{R}_i^{\alpha}$ denotes the position of the unit cell α in which the ith vertex is located (see ESI,† Section II). In our model, the unit of frequency is denoted by $\omega_0 = \sqrt{K_A \bar{A}/M_0}$, where K_A is the area modulus and has dimensions of Pa/m. M_0 is the mass of the typical cell, which is in the unit of kilogram.

3 Results

3.1 Band structure in homogeneous solid *vs.* fluid states

In a homogeneous tissue without mechanical heterogeneity, we find that the bandgaps only exist in fluid states. As shown in Fig. 2(a) and (b), when the shear modulus G vanishes at p_0 = 3.812, the bandgap $\Delta\omega$ shows up and keeps increasing deep into fluids. We take two typical states, solid at p_0 = 3.75 and fluid at p_0 = 3.9, and calculate the full band structures. The solid state has no bandgap (Fig. 2(c)) while the fluid has considerable bandgap (Fig. 2(d)). However, the fluid cannot transmit mechanical forces as a result of external perturbations due to the presence of floppy modes. For homogeneous solid states, increasing the cell perimeter elasticity K_P could enhance the rigidity, which means resulting in higher shear modulus and making the tissue more rigid. But there is no impact on the existence of bandgap (see ESI,† Fig. S1). Looking into the band structure, we find that the appearance of the bandgaps at the specific mode numbers is universal. The location of the bandgaps remains between mode N_E and N_E + 1, where N_E is the number of edges of the system. For a triple-junctional network, due to the Euler relation $N - N_E + N_V = 0$, the number of edges is 3 times of the cell number $N_E = 3N$ and the number of vertices is $N_V = 2N$. So the bandgaps always appear between mode $3N$ and $3N + 1$.

To obtain insights on the existence and behavior of the acoustic bandgaps in the vertex model, we consider the Hessian matrix of the system,

$$\begin{aligned} H_{i,j}^{\mu,\nu} &= \frac{\partial^2 E}{\partial r_i^{\mu} \partial r_j^{\nu}} \\ &= \sum_{m=1}^{N_E} \tau_m \frac{\partial^2 l_m}{\partial r_i^{\mu} \partial r_j^{\nu}} + K_P \sum_{\alpha=1}^{N} \frac{\partial P_{\alpha} \partial P_{\alpha}}{\partial r_i^{\mu} \partial r_j^{\nu}} + \mathcal{O}\left(\{A^i\}\right) \end{aligned} \tag{6}$$

The first term sums over all N_E edges where τ_m is the mechanical line tension for an edge m shared by cell i and j defined as eqn (2), and l_m is the edge length. The second term is positive definite and contributes a total count of N to rank(H). In a recent work by Yan and Bi,[54] they show that the area term has little impact on the counting rule while makes the decomposition of Hessian much more complicated. So we consider the special case when K_A = 0 without area contribution to the energy. In eqn (6), all area related terms come down to the infinitesimal part. Based on the above decomposition of the Hessian matrix, we can understand the existence of the bandgaps. The first N_E modes are induced by the first term and $N_E + 1 \rightarrow 2N_V$ higher modes come from the second term. For solid states, when upregulating K_P, tensions keep increasing and have no upper limits. Both of the two terms of eqn (6) are increasing which leads to the fact that all eigenmodes are shifting higher and no separation between eigenmodes emerges. For fluid states, the tension is saturating at high K_P values which means that the first term of eqn (6) remains almost constant while the second term keeps increasing with K_P. Therefore, the first N_E modes are almost unchanged and the $N_E + 1 \rightarrow 2N_V$ modes are moving higher when increasing K_P. The separation emerges between mode N_E and $N_E + 1$. That is why the bandgaps only exist in fluids between modes N_E and $N_E + 1$.

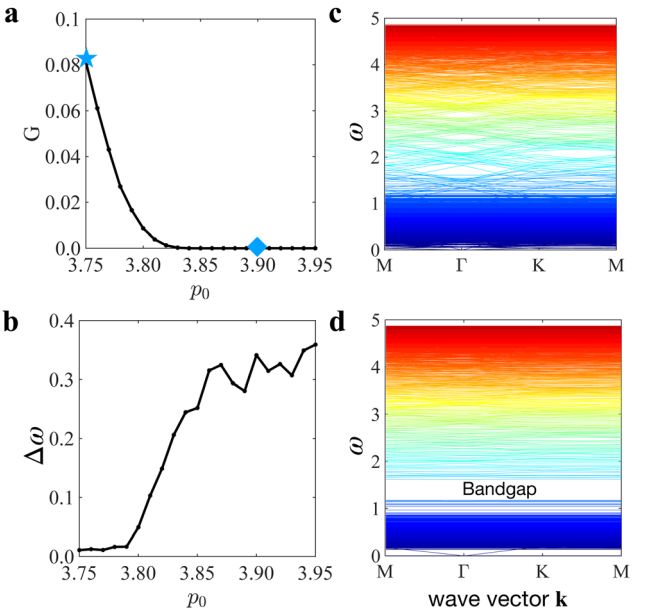

Fig. 2 Mechanical and acoustic properties for homogeneous tissues. We use N = 400 cell system with p_0 = 3.75 : 0.01 : 3.95, K_P = 1, K_A = 1. (a) Shear modulus G as a function of p_0. (b) Width of acoustic bandgap $\Delta\omega$ as a function of p_0. (c) Band structure for a solid state at p_0 = 3.75 indicated by blue asterisk in (a). ω is in units of $\omega_0 = \sqrt{K_A \bar{A}/M_0}$. (d) Band structure for a fluid state at p_0 = 3.9 indicated by blue diamond in (a). To obtain the full band structure, the dynamical matrix and eigenvalues are calculated along the $\vec{k}$ path $\mathbf{M} = \pi/L(1, 1/\sqrt{3}) \rightarrow \mathbf{\Gamma} = \pi/L(0,0) \rightarrow \mathbf{K} = \pi/L(1/3, 1/\sqrt{3}) \rightarrow \mathbf{M} = \pi/L(1, 1/\sqrt{3})$. $L = \sqrt{N}$ is the box size of the system.

3.2 Heterogeneous solids could realize both rigidity and bandgaps

Fig. 3(a) shows a typical snapshot of the heterogeneous tissue in the simulations. Colors represent various p_0 values of each cell. In our recent work studying how the heterogeneity affects

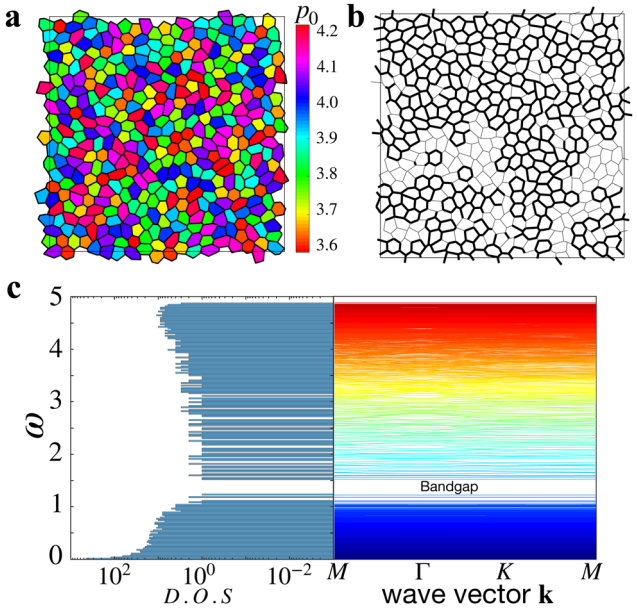

Fig. 3 Tissue structure and band structure in the vertex model simulations. (a) Colors represent various p_0 values of single cells. (b) Tension network of the heterogeneous solid state. Edges with finite tensions are indicated by thick black lines while other edges have $\tau = 0$. In this network, the tension percolation has occurred. (c) Density of states and band structure along wave vectors **k** for $N = 400$, $\mu = 3.87$, $\sigma = 0.1$, $K_P = 1$, $K_A = 1$.

the rigidity of a tissue, we find a very interesting intermediate state,[30,31] the heterogeneous solid (H. Solid), which has tension network percolation but no rigid cell contact percolation. A percolating tension network is shown in Fig. 3(b). The heterogeneous solids are consequences of the mechanical heterogeneity while for the homogeneous tissue, this intermediate state disappears. After the heterogeneity σ is introduced, the homogeneous fluids can be rigidified at some μ values. The critical value of μ that the rigidity transition occurs is determined by the strength of the heterogeneity σ. The density of states and band structure of a typical heterogeneous state are shown in Fig. 3(c). The illuminating behavior of the heterogeneous solids that it still has a sizable bandgap like the fluid state attracts our curiosity about properties of acoustic bandgaps in these systems.

As shown in Fig. 4(a), we plot the width of bandgaps $\Delta\omega$ and scaled shear modulus G/as a function of f_r. Here f_r represents the fraction of rigid cells with $p_0 < 3.812$. For a Gaussian distributed set of p_0 with mean μ and standard deviation σ, the fraction of rigid cells can be calculated $f_r = \frac{1}{2}\mathrm{erfc}\left(\frac{\mu - 3.812}{\sqrt{2}\sigma}\right)$. A very interesting crossover is found in Fig. 4(a) near the rigid cell contact percolation critical point $f_r^c = 0.48$. This behavior is quite similar with the scaled shear modulus as a function of μ presented in our previous work.[30] At the critical $f_r^c = 0.48$ where the contact percolation occurs, the width of the bandgaps is constant despite various σ values. The crossover separates the bandgaps into two mechanical regimes. On the left side of f_r^c, $\Delta\omega$ is increasing with σ which means heterogeneity σ enhances

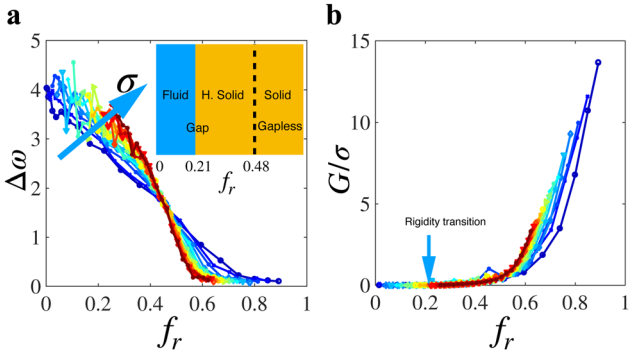

Fig. 4 Characterizing properties of acoustic band structures. (a) $\Delta\omega$ as a function of f_r at $N = 100$,$\sigma = 0.05:0.01:0.2$, $K_P = 10$, $K_A = 1$, $\mu = 3.75:0.01:3.95$. There is a crossover at $f_r \approx 0.48$ which coincides with the critical point of the rigid cell contact percolation. (inset)Phase diagram on where acoustic bandgaps exist. (b) Scaled shear modulus G/σ *vs.* f_r at $N = 100$, $\sigma = 0.05:0.01:0.2$, $K_P = 10$, $K_A = 1$, $\mu = 3.75:0.01:3.95$.

the bandgaps. However, when f_r is larger than f_r^c, $\Delta\omega$ is decreasing with σ indicating that the heterogeneity is suppressing the bandgap. In the inset of Fig. 4(a), a schemed phase diagram shows the existence of bandgaps for various heterogeneous tissue states. For the fluid state, there is a sizable bandgap. However, as mentioned above in Section 3.1, the fluid state is difficult for practical applications due to a number of floppy modes, which localize external excitations. For a pure rigid state at $\mu < 3.812$, there is no bandgap at all. In Fig. 4(b), the scaled shear modulus G/σ is plotted as a function of f_r. By comparison between $\Delta\omega$ and G/σ, we find that the heterogeneous solid states at $0.21 < f_r < 0.48$ are optimal candidates to obtain both rigidity and acoustic bandgaps. Now we have states with complete acoustic bandgaps, how to control the bandgaps and obtain gaps large enough? We will discuss these problems in the following section.

3.3 Cell perimeter elasticity could control the size of mechanical bandgaps

In the vertex model, K_P is the cell perimeter elasticity. Inspired by previous works[3,57,58] that the contrast of spring constants could generate mechanical band gaps in a spring network, we are wondering if it is possible to control acoustic bandgaps by tuning K_P in the vertex model. In this section, we calculate mechanical tensions and the width of acoustic bandgaps as a function of cell perimeter elasticity K_P at $N = 100$, $\sigma = 0.1$, $K_A = 1$ and various μ values. Remember that the rigidity transition occurs at $\mu \approx 3.9$ when the heterogeneity $\sigma = 0.1$.[30] As shown in Fig. 5(a), when $\mu < 3.812$, the systems are solid states and tensions τ keep increasing with K_P. In heterogeneous solids at $3.812 < \mu < 3.9$, τ also increase with K_P then saturate. In addition, increasing K_P largely promotes the size of bandgaps which can be seen in Fig. 5(b). The bandgaps $\Delta\omega$ keep monotonically increasing with K_P for heterogeneous solids and fluids at various μ values, showing similar power-law behaviors. As discussed in Section 3.1, $\Delta\omega$ also exist between modes N_E and $N_E + 1$ as the homogeneous tissues. This means that the cell perimeter elasticity K_P could change the width but not shift

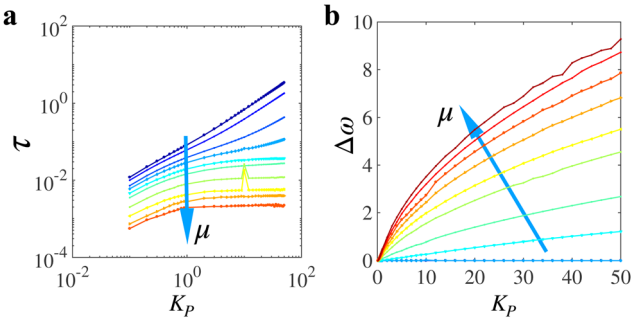

Fig. 5 Manipulating mechanical tensions and bandgaps. (a) Tension τ as a function of K_P at N = 100, K_A = 1, σ = 0.1, μ = 3.75, 3.77, 3.79, 3.80, 3.82, 3.83, 3.85, 3.87, 3.89, 3.90. The data is plotted at log–log scale. (b) $\Delta\omega$ as a funciton of K_P for the same state as in (a). $\Delta\omega$ is increasing with K_P for heterogeneous solids and fluids.

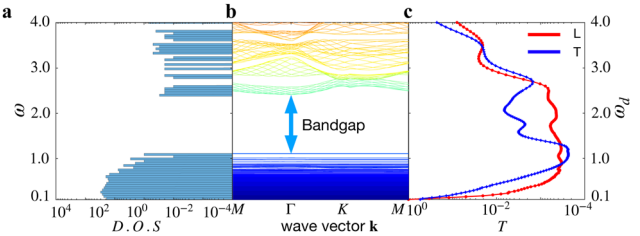

Fig. 6 Characterization of transmission properties for a heterogeneous solid state N = 100, μ = 3.815, σ = 0.1, K_P = 5, K_A = 1 excited by a sinusoidal wave $A\,sin(\omega_0 t)$. The damping coefficient b = 0.8 and amplitude A = 0.1. (a) Density of states. (b) Band structure along various wave vectors k. (c) Transmission coefficient T on the boundary for both transverse and longitude perturbations at various driven frequencies ω_d.

mode locations of the bandgaps. Note that increasing K_P and introducing heterogeneity into solid states at $\mu < 3.812$ do not generate bandgaps as shown in ESI,† Fig. S2.

3.4 Transmission coefficient to quantify the size and position of bandgaps

We have used the density of states and band structure to characterize the bands of the tissue and quantify the width of bandgaps. They are all static properties of the system and predictions based on linear response calculations. To further demonstrate the existence of the acoustic bandgap and explore the dynamical property of elastic wave transmission, we calculate the transmission coefficient[1,2,59,60] of the system perturbed by a sinusoidal wave excitation at various driven frequencies. The excitation is put at the center of the system. Both transverse and longitude oscillations are applied to the system. In the tissue, driven vertices evolve according to the overdamped equation of motion under longitude perturbation,

$$m_0\frac{d^2x}{dt^2} = \begin{cases} -b\dfrac{dx}{dt} + A\sin(\omega_d\, t) & \text{vertices of center cells} \\ -b\dfrac{dx}{dt} & \text{other vertices} \end{cases} \quad (7)$$

Here m_0 = 1 is the mass of a vertex, b is the damping coefficient, A is the amplitude of the perturbation and ω_d is the driven frequency. ω_d is in the unit of ω_0 which has been discussed in Section 2.2. For cells on the center, there is an external sinusoidal driving force $Asin(\omega_d t)$ and cells behave as driven oscillations. Other cells undergo damping oscillations. For a driven cell, all vertices on the cell are oscillating with the driven force. In Langevin dynamics, the damping force on vertices is $-b\boldsymbol{v}(x)$. Therefore, the power dissipated by the cell stripe located at x is $-b\boldsymbol{v}(x)^2$. By integrating the damping power at a time interval, we can get the energy dissipated by the vertices at position $\boldsymbol{x}$. The transmission coefficient T is defined as the ratio of the energy dissipated by the perturbed cells at the center of the system to the energy dissipated on boundary cells. We choose a typical heterogeneous solid state to calculate the transmission coefficient. The density of states and band structure are shown in Fig. 6(a) and (b). As shown in Fig. 6(c), at frequencies within the gaps, T drops to very low values for both transverse and longitude waves, indicating prohibited transmission of mechanical waves with these frequencies. In ESI,† Fig. S3, we make colormaps of transmission coefficient $T(x)$ for both transverse and longitude perturbations. $T(x)$ is the ratio of the energy dissipated at x to the energy dissipated on the boundary. We observe that the valley of the transmission coefficient of dynamical perturbations is consistent with the bandgaps predicted by the density of states and the band structures. This further demonstrates the existence of the bandgaps. For the heterogeneous solid states, whether the mechanical waves could be transmitted depends on the driven frequency ω_d. If the driven frequency is within the bandgap, the propagation of mechanical waves is prohibited, so the transmission coefficient vanishes. Outside the bandgap where mechanical waves could transmit through the system, the transmission coefficient could be finite values.

4 Discussions

In this work, we propose a design for amorphous 2D ABG materials that is inspired by how cells pack in dense tissues in biology. We generate structures that exhibit broad ABGs based on the vertex model that has been shown to describe cell shapes and tissue mechanical behavior. An advantage of this design is that the amorphous structure is more robust to defects and cell rearrangement. In addition, the width of ABGs can be directly tuned by mechanical parameter, say the cell perimeter elasticity K_P in heterogeneous solids. For a given heterogeneous solid state, increasing K_P largely enhances the width of the bandgap. The scaling relation between the width of the bandgap $\Delta\omega$ and K_P shows a universal cluster of the bandgaps. We use both static mechanical properties such as density of states, band structures, and dynamical transmission coefficients to characterize ABGs. The width and position of the bandgap are consistent for these results. In our tissue structure, there is a possible way to optimize the bandgaps by tuning the distribution of cell perimeter elasticity K_P based on a machine learning algorithm.[3] It will be straightforward to manufacture static acoustic materials based on this design using 3D printing or laser etching techniques. In addition, fabrication techniques

such as electron beam lithography or focused ion beam milling can also be used to precisely control the geometry and arrangement of micro/nanostructures based on the scale of the system. An even more exciting possibility is to adapt this design protocol to self-assemble structures. Recent advances in emulsion droplets have demonstrated feasibility to reconfigure the droplet network *via* tunable interfacial tensions and bulk mechanical compression. Researchers have shown that the amorphous biological tissue can be used as a template to design photonic materials.[23] Therefore, our protocol provides the possibility to construct the metamaterial with both acoustic and photonic bandgaps.

Code availability

The code for computing bandgaps and mechanical transmission is available upon reasonable request to the corresponding author.

Author contributions

Both X. L. and D. B. designed research, performed simulations, analyzed data and wrote the paper.

Conflicts of interest

There are no conflicts to declare.

Acknowledgements

We acknowledge support provided by the National Science Foundation DMR-2046683, the Sloan research fellowship from the Alfred P. Sloan Foundation, and the Northeastern University Discovery Cluster.

Notes and references

1 F. Warmuth, M. Wormser and C. Körner, *Sci. Rep.*, 2017, **7**, 3843.
2 Z. Jia, Y. Chen, H. Yang and L. Wang, *Phys. Rev. Appl.*, 2018, **9**, 044021.
3 H. Ronellenfitsch, N. Stoop, J. Yu, A. Forrow and J. Dunkel, *Phys. Rev. Mater.*, 2019, **3**, 095201.
4 Q. Wu, C. Cui, T. Bertrand, M. D. Shattuck and C. S. O'Hern, *Phys. Rev. E*, 2019, **99**, 062901.
5 H. Meng, N. Bailey, Y. Chen, L. Wang, F. Ciampa, A. Fabro, D. Chronopoulos and W. Elmadih, *Sci. Rep.*, 2020, **10**, 18989.
6 T. Vasileiadis, J. Varghese, V. Babacic, J. Gomis-Bresco, D. Navarro Urrios and B. Graczykowski, *J. Appl. Phys.*, 2021, **129**, 160901.
7 J. Jin, S. Jiang and H. Hu, *Rev. Adv. Mater. Sci.*, 2022, **61**, 68–78.
8 C. L. Willey, V. W. Chen, D. Roca, A. Kianfar, M. I. Hussein and A. T. Juhl, *Phys. Rev. Appl.*, 2022, **18**, 014035.
9 J. N. Kirchhof and K. I. Bolotin, *npj 2D Mater. Appl.*, 2023, **7**, 10.
10 S. Valiya Valappil, A. M. Aragón and H. Goosen, *Solid State Commun.*, 2023, **361**, 115061.
11 G. Gantzounis, M. Serra-Garcia, K. Homma, J. M. Mendoza and C. Daraio, *J. Appl. Phys.*, 2013, **114**, 093514.
12 L. Zigoneanu, B.-I. Popa and S. A. Cummer, *Nat. Mater.*, 2014, **13**, 352–355.
13 K. M. Ho, C. K. Cheng, Z. Yang, X. X. Zhang and P. Sheng, *Appl. Phys. Lett.*, 2003, **83**, 5566–5568.
14 T. Elnady, A. Elsabbagh, W. Akl, O. Mohamady, V. M. Garcia-Chocano, D. Torrent, F. Cervera and J. Sánchez-Dehesa, *Appl. Phys. Lett.*, 2009, **94**, 134104.
15 S. A. Cummer, *Science*, 2014, **343**, 495–496.
16 Z. Tian and L. Yu, *Sci. Rep.*, 2017, **7**, 40004.
17 F. Li, P. Anzel, J. Yang, P. G. Kevrekidis and C. Daraio, *Nat. Commun.*, 2014, **5**, 5311.
18 M. N. Armenise, C. E. Campanella, C. Ciminelli, F. Dell'Olio and V. M. Passaro, *Phys. Procedia*, 2010, **3**, 357–364.
19 F. Zangeneh-Nejad and R. Fleury, *Rev. Phys.*, 2019, **4**, 100031.
20 S. Kishore, R. Sujithra and B. Dhatreyi, *Mater. Today: Proc.*, 2021, **47**, 4700–4707.
21 Y.-i Nakajima, E. J. Meyer, A. Kroesen, S. A. McKinney and M. C. Gibson, *Nature*, 2013, **500**, 359–362.
22 L. Atia, D. Bi, Y. Sharma, J. A. Mitchel, B. Gweon, S. A. Koehler, S. J. DeCamp, B. Lan, J. H. Kim, R. Hirsch, A. F. Pegoraro, K. H. Lee, J. R. Starr, D. A. Weitz, A. C. Martin, J.-A. Park, J. P. Butler and J. J. Fredberg, *Nat. Phys.*, 2018, **14**, 613–620.
23 X. Li, A. Das and D. Bi, *Proc. Natl. Acad. Sci. U. S. A.*, 2018, **115**, 6650–6655.
24 D. Zhou, J. Ma, K. Sun, S. Gonella and X. Mao, *Phys. Rev. B*, 2020, **101**, 104106.
25 H. Liu, D. Zhou, L. Zhang, D. K. Lubensky and X. Mao, *Soft Matter*, 2021, **17**, 8624–8641.
26 M. Charara, K. Sun, X. Mao and S. Gonella, *Phys. Rev. Appl.*, 2021, **16**, 064011.
27 T. Nagai and H. Honda, *Philos. Mag. B*, 2001, **81**, 699–719.
28 R. Farhadifar, J.-C. Röper, B. Aigouy, S. Eaton and F. Jülicher, *Curr. Biol.*, 2007, **17**, 2095–2104.
29 G. Duclos, S. Garcia, H. G. Yevick and P. Silberzan, *Soft Matter*, 2014, **10**, 2346–2353.
30 X. Li, A. Das and D. Bi, *Phys. Rev. Lett.*, 2019, **123**, 058101.
31 T. Fuhs, F. Wetzel, A. W. Fritsch, X. Li, R. Stange, S. Pawlizak, T. R. Kießling, E. Morawetz, S. Grosser, F. Sauer, J. Lippoldt, F. Renner, S. Friebe, M. Zink, K. Bendrat, J. Braun, M. H. Oktay, J. Condeelis, S. Briest, B. Wolf, L.-C. Horn, M. Höckel, B. Aktas, M. C. Marchetti, M. L. Manning, A. Niendorf, D. Bi and J. A. Käs, *Nat. Phys.*, 2022, **18**, 1510–1519.
32 J. A. Mitchel, A. Das, M. J. O'Sullivan, I. T. Stancil, S. J. DeCamp, S. Koehler, O. H. Ocaña, J. P. Butler, J. J. Fredberg and M. A. Nieto, *et al.*, *Nat. Commun.*, 2020, **11**, 1–14.
33 D. B. Staple, R. Farhadifar, J. C. Röper, B. Aigouy, S. Eaton and F. Jülicher, *Eur. Phys. J. E: Soft Matter Biol. Phys.*, 2010, **33**, 117–127.

34 B. Li and S. X. Sun, *Biophys. J.*, 2014, **107**, 1532–1541.
35 A. G. Fletcher, M. Osterfield, R. E. Baker and S. Y. Shvartsman, *Biophys. J.*, 2014, **106**, 2291–2304.
36 S. Kim and S. Hilgenfeldt, *Soft Matter*, 2015, **11**, 7270–7275.
37 D. Bi, J. H. Lopez, J. M. Schwarz and M. L. Manning, *Nat. Phys.*, 2015, **11**, 1074–1079.
38 L. Hufnagel, A. A. Teleman, H. Rouault, S. M. Cohen and B. I. Shraiman, *Proc. Natl. Acad. Sci. U. S. A.*, 2007, **104**, 3835–3840.
39 S. M. Zehnder, M. Suaris, M. M. Bellaire and T. E. Angelini, *Biophys. J.*, 2015, **108**, 247–250.
40 J.-A. Park, J. H. Kim, D. Bi, J. A. Mitchel, N. T. Qazvini, K. Tantisira, C. Y. Park, M. McGill, S.-H. Kim, B. Gweon, J. Notbohm, R. Steward, S. Burger, S. H. Randell, A. T. Kho, D. T. Tambe, C. Hardin, S. A. Shore, E. Israel, D. A. Weitz, D. J. Tschumperlin, E. P. Henske, S. T. Weiss, M. Lisa Manning, J. P. Butler, J. M. Drazen and J. J. Fredberg, *Nat. Mater.*, 2015, **14**, 1040–1048.
41 M. Plodinec, M. Loparic, C. A. Monnier, E. C. Obermann, R. Zanetti-Dallenbach, P. Oertle, J. T. Hyotyla, U. Aebi, M. Bentires-Alj, R. Y. H. Lim and C.-A. Schoenenberger, *Nat. Nanotechnol.*, 2012, **7**, 757–765.
42 Y. Fujii, Y. Ochi, M. Tuchiya, M. Kajita, Y. Fujita, Y. Ishimoto and T. Okajima, *Biophys. J.*, 2019, **116**, 1152–1158.
43 X. Guo, K. Bonin, K. Scarpinato and M. Guthold, *New J. Phys.*, 2014, **16**, 105002.
44 A. Fritsch, M. Höckel, T. Kiessling, K. D. Nnetu, F. Wetzel, M. Zink and J. A. Käs, *Nat. Phys.*, 2010, **6**, 730–732.
45 G. Ciasca, T. E. Sassun, E. Minelli, M. Antonelli, M. Papi, A. Santoro, F. Giangaspero, R. Delfini and M. De Spirito, *Nanoscale*, 2016, **8**, 19629–19643.
46 D. M. Sussman, *Comput. Phys. Commun.*, 2017, **219**, 400–406.
47 M. S. Hutson, Y. Tokutake, M.-S. Chang, J. W. Bloor, S. Venakides, D. P. Kiehart and G. S. Edwards, *Science*, 2003, **300**, 145–149.
48 M. Rauzi, P. Verant, T. Lecuit and P.-F. Lenne, *Nat. Cell Biol.*, 2008, **10**, 1401–1410.
49 G. W. Brodland, V. Conte, P. G. Cranston, J. Veldhuis, S. Narasimhan, M. S. Hutson, A. Jacinto, F. Ulrich, B. Baum and M. Miodownik, *Proc. Natl. Acad. Sci. U. S. A.*, 2010, **107**, 22111–22116.
50 K. K. Chiou, L. Hufnagel and B. I. Shraiman, *PLoS Comput. Biol.*, 2012, **8**, 1–9.
51 S. Ishihara and K. Sugimura, *J. Theor. Biol.*, 2012, **313**, 201–211.
52 S. Ishihara, K. Sugimura, S. J. Cox, I. Bonnet, Y. Bellaïche and F. Graner, *Eur. Phys. J. E: Soft Matter Biol. Phys.*, 2013, **36**, 45.
53 G. W. Brodland, J. H. Veldhuis, S. Kim, M. Perrone, D. Mashburn and M. S. Hutson, *PLoS One*, 2014, **9**, 1–15.
54 L. Yan and D. Bi, *Phys. Rev. X*, 2019, **9**, 011029.
55 X. Yang, D. Bi, M. Czajkowski, M. Merkel, M. L. Manning and M. C. Marchetti, *Proc. Natl. Acad. Sci. U. S. A.*, 2017, **114**, 12663–12668.
56 C. E. Maloney and A. Lematre, *Phys. Rev. E: Stat., Nonlinear, Soft Matter Phys.*, 2006, **74**, 016118.
57 Y. Zhou, P. R. Bandaru and D. F. Sievenpiper, *New J. Phys.*, 2018, **20**, 123011.
58 T. Kariyado and Y. Hatsugai, *Sci. Rep.*, 2015, **5**, 18107.
59 Z. G. Wang, S. H. Lee, C. K. Kim, C. M. Park, K. Nahm and S. A. Nikitov, *J. Appl. Phys.*, 2008, **103**, 064907.
60 G. Gkantzounis, T. Amoah and M. Florescu, *Phys. Rev. B*, 2017, **95**, 094120.